# Intra-Operative 2-D Ultrasound and Dynamic 3-D Aortic Model Registration for Magnetic Navigation of Transcatheter Aortic Valve Implantation

Zhe Luo, Junfeng Cai, Terry M. Peters, *Fellow, IEEE*, and Lixu Gu*, *Senior Member, IEEE*

***Abstract*—We propose a navigation system for transcatheter aortic valve implantation that employs a magnetic tracking system (MTS) along with a dynamic aortic model and intra-operative ultrasound (US) images. This work is motivated by the desire of our cardiology and cardiac surgical colleagues to minimize or eliminate the use of radiation in the interventional suite or operating room. The dynamic 3-D aortic model is constructed from a preoperative 4-D computed tomography dataset that is animated in synchrony with the real time electrocardiograph input of patient, and then preoperative planning is performed to determine the target position of the aortic valve prosthesis. The contours of the aortic root are extracted automatically from short axis US images in real-time for registering the 2-D intra-operative US image to the preoperative dynamic aortic model. The augmented MTS guides the interventionist during positioning and deployment of the aortic valve prosthesis to the target. The results of the aortic root segmentation algorithm demonstrate an error of $0.92 \pm 0.85$ mm with a computational time of $36.13 \pm 6.26$ ms. The navigation approach was validated in porcine studies, yielding fiducial localization errors, target registration errors, deployment distance, and tilting errors of $3.02 \pm 0.39$ mm, $3.31 \pm 1.55$ mm, $3.23 \pm 0.94$ mm, and $5.85 \pm 3.06^\circ$, respectively.**

***Index Terms*—Aortic root contour extraction and feature based registration, dynamic aortic model, intra-operative US image, magnetic navigation.**

## I. INTRODUCTION

SYMPTOMATIC aortic stenosis is the most frequent valvular disease in older patients (affecting nearly 5% of the population aged over 75 [1]), and is associated with predictable clinical deterioration and poor survival in the absence of aortic valve replacement. Surgical replacement of the aortic valve is required to treat symptoms and improve survival in patients with aortic stenosis [2]. However, many patients with severe symptomatic aortic stenosis cannot undergo surgical valve replacement because of advanced age or significant comorbidities [3]. Transcatheter aortic valve implantation (TAVI) is a new procedure that is a less invasive alternative to open heart surgery. TAVI delivers a bioprosthetic valve via a catheter that is inserted into the aorta through the femoral artery, or via the apex of the left ventricle, to approach, displace, and replace the native valve. This minimally invasive procedure enables valve replacement to be performed without the need for a median sternotomy or cardiopulmonary bypass [4], and has consequently become a feasible alternative for high risk patients.

Accurately positioning the valve during deployment is paramount for the success of the procedure [5]. Malpositioning of the valve can lead to migration, coronary obstruction, paravalvular leakage, atrioventricular block, or aortic root rupture [6]. Most TAVI procedures depend solely on single plane fluoroscopic imaging to position the new valve in the aortic root during deployment. While contrast-enhanced fluoroscopy is commonly used to visualize the aortic anatomy and valve stent during guidance of the procedure [7], it can only provide poorly visualized images of the aortic valve without the appropriate 3-D context that could help physicians to more accurately define the target, giving rise to navigational limitations that may result in the malpositioning of the valve [8]. In addition, fluoroscopy also can expose the clinicians, staff, and patient to excessive levels of ionizing radiation. According to feedback from our collaborating physicians, due to the high patient load in China, each interventionist performs thousands of cases during their careers, and has identified radiation as the dominant area of concern during this procedure. Moreover, the use of contrast agent increases the risk of iatrogenic renal injury [9]. Therefore, an alternative image-guidance procedure that mitigates these limitations is needed for TAVI.

Preoperative computed tomography (CT) or magnetic resonance (MR) images are capable of producing detailed and comprehensive images of the beating heart and are readily available for viewing in the operating room (OR). Lauritsch *et al.* [10] discussed the advancements in C-arm computed tomography and demonstrated the feasibility of C-arm guidance during simulation in both an experimental phantom and in preclinical *in vivo* studies. Kempfert *et al.* [11] have used DynaCT (a C-arm CT system) augmented fluoroscopy to improve the deployment precision and to successfully guide TAVI in 50 patients. Although the technique can distinguish bones from soft tissues, CT images show only small contrast differences in the anatomy of the heart, and require the use of X-ray contrast to adequately delineate the cardiac chambers. Moreover, this approach still exposes

---

Manuscript received May 14, 2013; revised July 25, 2013; accepted July 25, 2013. Date of publication July 30, 2013; date of current version October 28, 2013. This work was supported in part by the Chinese NSFC research fund (61190120, 61190124 and 61271318), in part by the Shanghai Municipal Health Bureau research fund (2011216) and Biomedical engineering fund of Shanghai Jiao Tong University (YG2012MS21), and in part by the Canadian Institutes of Health Research (MOP179298). *Asterisk indicates corresponding author.*

Z. Luo is with the Image Guided Surgery and Therapy Laboratory, School of Biomedical Engineering, Shanghai Jiao Tong University, Shanghai 200030, China (e-mail: luozhe2007@hotmail.com).

J. Cai, is with the Department of Cardiac Surgery, Ruijin Hospital, Shanghai Jiao Tong University, Shanghai 200030, China (e-mail: lonlon_cn@hotmail.com).

T. Peters is with the Imaging Research Laboratories, Robarts Research Institute, Western University, London, ON N6A 5K8 Canada (e-mail: tpeters@robarts.ca).

*L. Gu is with the Image Guided Surgery and Therapy Laboratory, School of Biomedical Engineering, Shanghai Jiao Tong University, Shanghai 200030, China (e-mail: gulixu@sjtu.edu.cn).

Digital Object Identifier 10.1109/TMI.2013.2275233

the interventionist and patient to harmful radiation. Recently, some researchers also addressed the issue of catheter tracking and fusion between fluoroscopic images and US for TAVI procedures [12], [13] to provide better 3-D context of the target. Although radiation reduction was not achieved, there was improved understanding of the intra-operative anatomical structure of the target region. Horvath *et al.* [14], [15] employed real-time MRI to obtain excellent visualization of anatomical features and achieved TAVI on porcine models, but still faced a number of implementation issues, including restricted surgical access, incompatibility with conventional surgical instruments, and increased expense and complexity of procedures, which limit its spread in clinical application.

When the surgical instrument is appropriately equipped with sensors, a magnetic tracking system (MTS) can provide spatial information on the pose of the instruments and ultrasound transducers, and in patient coordinates during surgery. The use of an MTS allows the preoperative 3-D CT (MRI) to be registered to the patient coordinate system so that the relative position and orientation of the anatomical structure defining the surgical target can be represented in patient-centered coordinates. This allows the intervention to be guided using magnetically-tracked instruments rather than relying on X-ray guidance. Manstad–Hulaas *et al.* [16] employed navigation technology to deploy stent-grafts for treatment of side-branched abdominal aortic aneurysms in phantoms. Abi–Jaoudeh *et al.* [17] performed thoracic stent-graft deployment in three swine using MTS navigation alone and presented an analysis of accuracy and feasibility. However, the use of MTS alone cannot recover movements of the aortic root during surgery, which results in poor registration accuracy and therefore limits the ability to precisely deploy aortic valve prostheses.

Due to its safety, comparative low cost, ease of use, minimal disruption to the procedure, and lack of compatibility problems between US imaging and standard OR equipment [18], US imaging is an attractive complement to CT and MRI during surgery. In addition, real-time US imaging can provide information relating to the surgical target region in real time. Huber *et al.* [19] reported the use of simultaneous intracardiac and intravascular US in an animal model to navigate an off-pump aortic valve stent implantation. However, the limited resolution and field of view make the US images difficult to interpret. To improve the interpretability of US images, Lang *et al.* [20] constructed an augmented image-guidance system for TAVI by registering together 3-D trans-esophageal echo (TEE) ultrasound and a static cardiac model derived from preoperative CT, and then evaluating the system on human image data. However, since the aortic root model was stationary, the final precision of valve placement could be compromised. Real-time 3-D US is still a relatively new and expensive procedure compared to 2-D US and limited access to the streaming 3-D data makes it impractical to perform real-time fusion with other images. On the other hand, real-time 2-D US imaging (cardiac echo), such as TEE and transthoracic echocardiography (TTE), has relatively high spatial and temporal resolution, and is readily available since it is routinely employed during cardiac interventions as a monitoring modality.

MTS, combined with intra-operative 2-D US and preoperative 3-D imaging, would provide the surgeon with complementary information captured in two different modalities, greatly facilitating the interpretation of the images. Our previous work [21] performed thoracic aortic stent-graft deployment using MTS combined with intra-operative 2-D US image and validated the combined system using phantom and animal studies. To obtain visualization of anatomical features equivalent to that demonstrated by Horvath using intra-operative MRI [14], [15], and to achieve a more accurate registration, we developed a prototypical navigation system [22] registering a preoperative dynamic aortic model to the intra-operative US image for TAVI and validated the feasibility of the whole procedure.

This paper extends our pilot study [22] through the introduction of a novel algorithm for electrocardiograph (ECG) signal phase calculation, temporal synchronization and aortic root extraction from US images. We use an intra-operative US image, registered to a dynamic aortic surface model derived from preoperative 4-D CT, as an alternative means of intra-operative TAVI guidance. The deployment of the aortic valve prosthesis is guided by a multimodality navigation system that integrates an MTS-tracked 2-D US image with its 3-D context, by registering it to a preoperative dynamic aortic model derived from preoperative 4-D CT images. The dynamic 3-D aortic model is constructed from the preoperative 4-D CT image, which is animated with reference to the patient's real time electrocardiograph (ECG) signal, and preoperative planning is performed to determine the target position of the aortic valve prosthesis. US probe calibration is performed to calculate the transformation that maps the US image coordinate to the tracked device coordinate, following the introduction of a real time US image into the system. Following the automatic real-time extraction of the contours of the aortic root from the short axis US images, a feature-based registration is employed to register the 2-D intra-operative US image to the preoperative dynamic aortic model, thus mapping the preoperative CT image to the intra-operative US. Finally, the augmented MTS system guides the interventionist to the appropriate location to deploy the prosthesis to the target. Compared to the similar work of Lang *et al.* [20], this research employs a dynamic aortic model, to which the intra-operative US image is registered to achieve better registration accuracy. Fluoroscopy was not used at any time during the procedure.

## II. MATERIALS AND METHOD

### A. Dynamic Aortic Model

The dynamic aortic model was constructed based on the 4-D CT image of the beating heart acquired over a cardiac cycle with retrospective ECG gating. Ten high resolution contrast-enhanced 3-D CT image volumes, spanning a complete cardiac cycle, were acquired using a TOSHIBA Aquiline ONE CT scanner with the following imaging parameters: slice thickness $= 0.5$ mm; pitch $= 0.237$; kVp$=$ 120; mA $=$ 132; field of view $=$ 22 cm; image matrix $= 512 \times 512$; voxel dimensions and $= 0.653$ mm $\times$ 0.653 mm $\times$ 0.25 mm. For each CT image, a manual segmentation was performed slice-by-slice using a "paint pen" technique to outline the aortic structure, which was then reconstructed using Marching Cubes [23]. Finally, the dynamic aortic model consisted of 10 static models (Fig. 1). These phases were equally sampled in time. While it may be benefi-

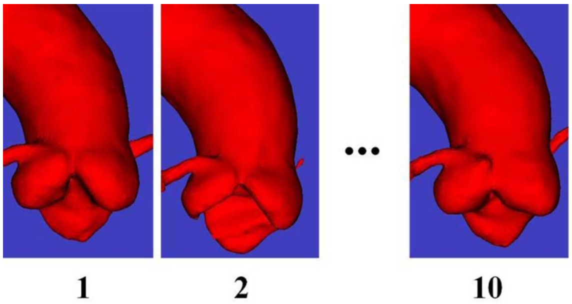

Fig. 1. Dynamic aortic model of a cardiac cycle extracted from CT.

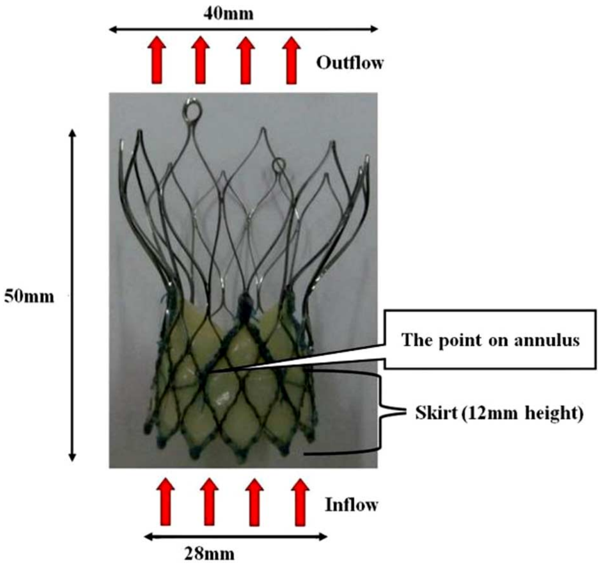

Fig. 2. Transcatheter aortic valve prosthesis. Pericardial skirt, which is designed to prevent paravalvular regurgitation, covers the lower segment of the aortic valve prosthesis from the inflow to the annulus.

cial to obtain more accurate registration by choosing more samples during the phases that exhibit the most cardiac motion, as demonstrated in Table IV, it is more robust to register US and CT images at diastole due to fewer motion artifacts, and specifically at mid-diastole to obtain optimum accuracy across the cardiac cycle. It is therefore more feasible to register the US and CT images at diastole and apply the resultant transformation throughout the cardiac cycle.

### B. Preoperative Planning

Prior to the procedure, the surgeon must determine the optimal position of the prosthesis relative to the preoperative images. The structure of the prosthesis, which has an annulus, is shown in Fig. 2. For each preoperative CT image, the surgeon manually identifies the three points on the annulus defined by the lowest points of the leaflets, [Fig. 3(a)] to determine the annular plane [Fig. 3(b)]. The annular plane is then translated along its normal path towards the left ventricle (LV) with a translation distance of about half of the height of the skirt (6 mm). The final plane is defined as the target position [Fig. 3(b)] in the dynamic aortic model. During the navigation procedure, since the intra-operative US, MTS and the preoperative model were registered together, we just need to measure the difference between the orientation of the tracked catheter and the normal of the target plane.

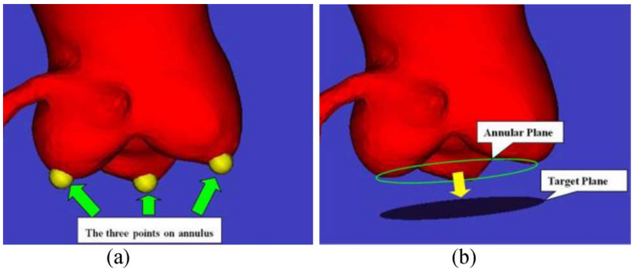

Fig. 3. Preoperative planning. (a) The three points of the annulus (the yellow dots). (b) The annular plane (green circle) defined by the three yellow dots. This plane is translated towards the LV by 6 mm to obtain the final target plane (dark disc).

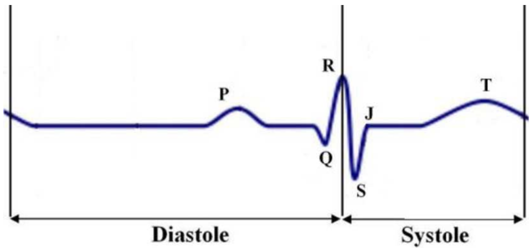

Fig. 4. R wave in the ECG waveform.

### C. Calculation of Cardiac Phase From ECG Signals

The ECG recorder communicates with the system via a serial port at 38 400 Hz transmitting 17 bytes of data to the system, 62 times per second (about 16 ms/sample). Each data packet contains four ECG signals at approximately 4 ms intervals. A queue data structure is used to record the input signals. When a new signal is about to be appended to the rear of the queue, the first element is ejected and the new signal is added if the queue is full.

As shown in Fig. 4, the R wave is one of the most distinctive elements in the ECG signal, having the largest magnitude gradients (of opposite sign) on each side.

We define the gradient product $g(t)$ as

$$g(t) = \frac{(E(t) - E(t - \Delta t))(E(t) - E(t + \Delta t))}{\Delta t^2} \qquad (1)$$

where $t$ is time, and $E(t)$ is the ECG signal. $g(t)$ is maximum when $t$ coincides with R. We define R as the beginning of each cardiac cycle. For each input data element, we check whether the sample containing R lies within the input queue. If R is present, we update the cardiac cycle period with this point as the beginning of the new cycle, otherwise we find the previous R point in the queue and base the current cardiac phase on it instead. The calculated cardiac phase is therefore based on the last ECG signal of new input data. Algorithm 1 (see Appendix) describes the details of cardiac phase calculation from ECG signals. In computing the cardiac phase, we assume that the subject's cardiac period is stable. Initially, we use the queue data structure to reserve a set number of ECG signals to calculate the average cardiac period, which is then established as the initial cardiac cycle period. Since each data packet contains four ECG signals at approximately 4 ms intervals, the difference between $i$ and $j$ was multiplied by 4 represents the time duration between the point $i$ and $j$.

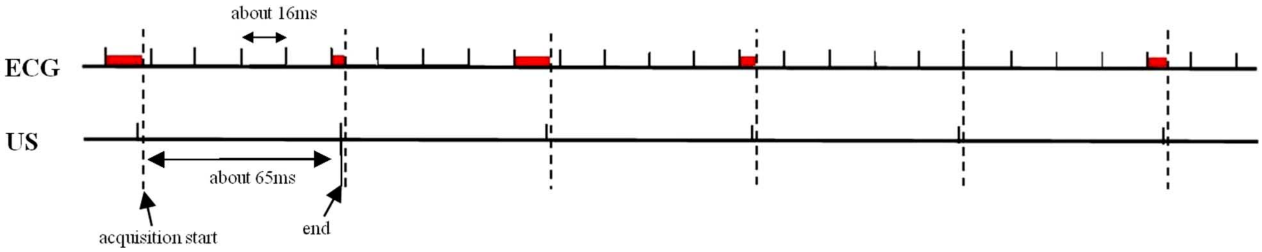

Fig. 5. Diagram of the acquisition latency of the US image. Besides the US image, the figure illustrates the sample times of the ECG signals. For each US image, the left end of the bold red line is the cardiac phase at which the image was acquired, and the right end is its actual cardiac phase. Length of red bold line is the error of this cardiac phase.

### D. Temporal Synchronization Mechanism

As shown in Fig. 5, there are two aspects related to the synchronization of the data streams associated with the different sampling delays in the US image, ECG signal and spatial tracking information acquisition. Due to the different latencies of these data sources, readings from different inputs, even if they are made at the same time, may not correspond to the same cardiac phase. In this paper, latency is defined as the period between the commencement of the data collection and when the data are reported to the processing system. Because the sampling delay of the spatial tracking information, i.e., the position and orientation information of the sensors mounted on the cannula, catheter and the US probe respectively, is less than 0.1 ms in our system, this effect can be ignored.

In this system, synchronization, ECG acquisition, and US image acquisition threads are created to acquire the ECG signals and US image in parallel. The US and ECG signal threads are synchronized by the synchronization thread. The ECG acquisition thread acquires real-time ECG signals of the subject from the ECG recorder through a serial port, analyzes the corresponding cardiac phase of the current input ECG signal and writes the cardiac phase to a public buffer about 62 times/s. The US acquisition thread acquires a US image from the US machine after it obtains the acquisition notification from the synchronization thread. For each update time, the synchronization thread reads the current cardiac phase from the public buffer, and acquires the spatial tracking information from the Aurora MTS. It then converts the tracking information into a 4 × 4 matrix containing the position and orientation information of sensors mounted on the cannula, catheter, and the US probe. The time to perform these operations is negligible. The synchronization thread then notifies the US acquisition thread to acquire a new US image, after which it saves the image in the public buffer, and signals the completion of US acquisition. The spatial tracking information and cardiac phase acquired by the synchronization thread are considered synchronous with the US image. Finally, the synchronization thread sends the cardiac phase and spatial tracking information to the registration thread (mentioned in "software" section). Since the latency of US is not exactly 65 ms, we didn't use it as constant displacement for better accuracy in our application.

While Huang *et al.* [18] proposed a method to align the ECG signals, intra-operative US images, and spatial tracking information, their approach required a costly additional dynamic cardiac phantom. (We note that improvements to the NDI tracking system have now largely eliminated the tracking latency reported by Huang). Here, we present a simplified method to accomplish the temporal alignment between the three input sources for more efficient implementation in the clinic. Since the acquisition latency of the spatial tracking information in our implementation is negligible, temporal synchronization consists mainly of the alignment between the US images and the ECG signals. As shown in Fig. 5, the error of the temporal alignment comes from the latency between the start point of US image acquisition and the closest start point of an ECG signal sample preceding it. For ECG signals with a sample interval of 16 ms, the error is less than 16 ms. In the following, $T_U$ is the period of acquisition of a US image and $T_E$ is the time between two ECG signals. The US acquisition thread and ECG signals acquisition threads begin acquiring data at approximately the same time. For the $N$th US image, we set the $M$th ECG signal as its counterpart. So we have

$$T_E M \leq T_U N \tag{2}$$

$$M \leq \frac{T_U N}{T_E} \tag{3}$$

where $M$ is the largest integer satisfying inequality (3). So we have

$$\text{error} = \left( \frac{T_U N}{T_E} - \left\lfloor \frac{T_U N}{T_E} \right\rfloor \right) T_E. \tag{4}$$

The error actually is the fractional part of $(T_U N)/(T_E)$. Let $T_U = aT_E + b, 0 \leq b < T_E$, where $a$ and $b$ are integers. Therefore $(T_U N)/(T_E) = ((aT_E + b)N)/(T_E) = aN + (b)/(T_E)N$. For the case where $a$ and $N$ are integers, we only need to consider $(bN)/(T_E)$. If we denote $r$ to be the remainder of $(bN)/(T_E)$, we obtain the error as $rT_E$. Since the average $r$ is $(T_E)/(2)$, we obtain $\text{error}_{\text{average}} = (T_E/2)/(T_E)T_E = (T_E)/(2) = 8$ ms.

In comparison to Huang's work [18], our method may have lower accuracy, but in our experience, it is simpler, faster and convenient for clinical application.

In the animal study, a constant heart rate in the pig models was ensured by injecting Betaloc (5 mg:5 ml, Vetter Pharma-Fertigung Gmbh & CoKG, Germany). In some cases however, the heart rate may change significantly. To address this issue, as shown by Algorithm 1, the cardiac phase calculation algorithm uses the period of most recent cardiac cycle to update the current cardiac period and calculate the correct cardiac phase of the current input ECG signal.

### E. Aortic Root Contour Extraction

We describe below a novel segmentation algorithm to extract the contour of the aortic valve from the intra-operative US image, which is used to register to preoperative dynamic aortic model intra-operatively using feature based registration. This algorithm employs a novel energy function construction method and novel postoperative image processing to obtain the accurate aortic root contour in short axis US images in real time.

*Continuous Max-Flow Image Segmentation:* The image segmentation problem with respect to an image with two regions can be described as a minimization problem of an energy function [24]

$$\arg\min_{\lambda\in[0,1]} E(\lambda) = \int_\Omega (1-\lambda(x))C_s(x)\,dx + \int_\Omega \lambda(x)C_t(x)\,dx + \alpha\int_\Omega |\nabla\lambda(x)|\,dx \quad (5)$$

where

$\lambda(x) \in [0,1]$ is a labeling function which labels an image pixel $x$ as foreground or background and $C_s(x)$ and $C_t(x)$ are the regional penalties that assign a pixel as foreground and background respectively based on image properties;

$|\nabla\lambda(x)|$ is the total variation of the labeling function, and $\alpha$ defines the relative weight of the image property and smoothness constraint.

Here, we use a continuous max-flow algorithm [25] to segment the aortic valve of the US image. Compared to classic graph-cut based methods, continuous max-flow can avoid grid bias, increase the segmentation accuracy and can be implemented and parallelized by a graphics processing unit (GPU) [26]. This approach makes the algorithmic solver much faster than graph cuts and allows the aortic root to be segmented in approximately real-time.

*Probability Estimate:* Prior to constructing the energy function, we compute the probability distributions of prior images based on both intensity and distance. Based on the probability distribution, low intensity pixels near the center of prior segmentations are more likely to be identified as foreground, while high intensity pixels far from the center are more likely to be labeled as background.

We obtain 5–7 evenly-spaced *prior* images from the US video signal obtained over a single cardiac cycle, segment the contours of the aortic roots manually so that each image represents a different cardiac phase, and calculate a bounding box for each segmentation result. A maximum bounding box is determined using these individual boxes. Based on the segmented *prior* images, a probability function is generated by calculating the conditional probability [20] of a pixel identified as foreground, using intensity and distance to the center point, and the geometric mean of all centers of the *prior* images, as shown in Fig. 6(a) and (6)

$$P(x) = P(F(x)|R(x),I(x)) = \frac{1}{n}\sum_{i=1}^{n}\frac{P(F_i\cap R(x),I(x))}{P(R(x),I(x))} \quad (6)$$

where $P(F_i)$ is the probability that a pixel belongs to the foreground, and $P(R,I)$ the probability that a pixel's intensity and distance to the center are $I$ and $R$ respectively, and $n$ is the number of *prior* images.

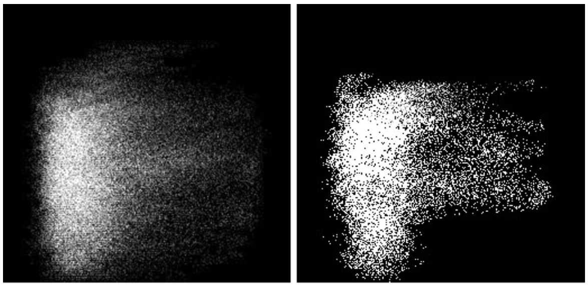

(a) (b)

Fig. 6. Probability function generated from the prior US images. (a) Using the geometric center of all prior images' segmentation centers. (b) Using the geometric center of one of the segmented prior images.

For each *prior* image, a probability function [Fig. 6(b)] is also generated by calculating the conditional probability of a pixel identified as foreground using intensity and distance to the center point of its segmented version

$$P_i(x) = P(F(x)|R(x),I(x)) = \frac{P(F\cap R(x),I(x))}{P(R(x),I(x))} \quad (7)$$

where $P_i(x)$ is the probability function of the $i$th *prior* image.

*Energy Function Construction:* For each input short axis US image, we construct the energy function described below

$$C_s(x) = |I_x - I_F| \quad (8)$$

$$C_t(x) = |I_x - I_B| \quad (9)$$

$$C_p(x) = 0.5 \quad (10)$$

where $x$ is the position of a pixel, $C_s$ and $C_t$ are the data items representing foreground and background, respectively, and $C_p$ is a smoothness term. $I_F$ and $I_B$ are the intensities most representative of the foreground and background as defined below.

For each *prior* image $i$, we calculate its $I_F^i$ and $I_B^i$ respectively using

$$I_F^i = \sum_{p\in F} I(p)P^F_{I(p)} \quad (11)$$

$$I_B^i = \sum_{p\in B} I(p)P^B_{I(p)} \quad (12)$$

where $F$ and $B$ are the foreground and background regions, $I(p)$ is the intensity of pixel $p$, and $P_I^F$ and $P_I^B$ are the probabilities of intensity $I$ in the foreground and background regions, respectively.

The probability map of the current input US image [Fig. 7(a)] is obtained by the probability function $P(x)$ as shown in Fig. 7(b). The Otsu threshold algorithm [27] was applied to the probability map to obtain an optimal threshold $T$. Pixels with values $<T$ were removed, with the remainder comprising the target region $A$ [Fig. 7(c)]. Finally, the centroid of the remaining pixels was defined as the center $C$ of the target region. Each *prior* image $i$ ($1\le i\le N$, $N$ is number of *prior* images) was then used to determine its similarity with the current input US image. The similarity metric (SM) employed is defined as

$$\mathrm{SM}_i = \sum_{p\in A}\sqrt{\left(D_p - D_p^i\right)^2 + \left(I_p - I_p^i\right)^2} \quad (13)$$

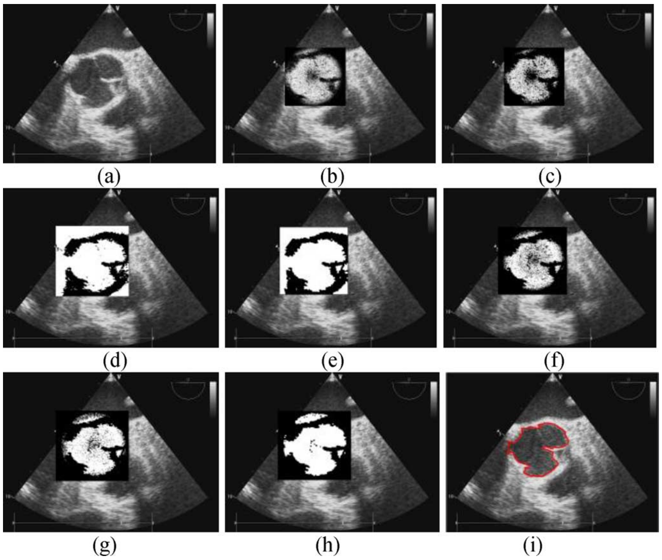
(a) (b) (c) (d) (e) (f) (g) (h) (i)

Fig. 7. Process of aortic root extraction in the short axis US image. (a) Original image. (b) Probability function of the current US image. (c) Result of the Otsu operation to calculate the geometric center of the target region. (d) Result after segmentation using continuous max flow. (e) The result after open and close operations. (f) Result of multiplying the image in (e) by the probability function. (g) Result after thresholding (f). (h) Result of the open and close operation on the result of (g). (i) Final extracted contour.

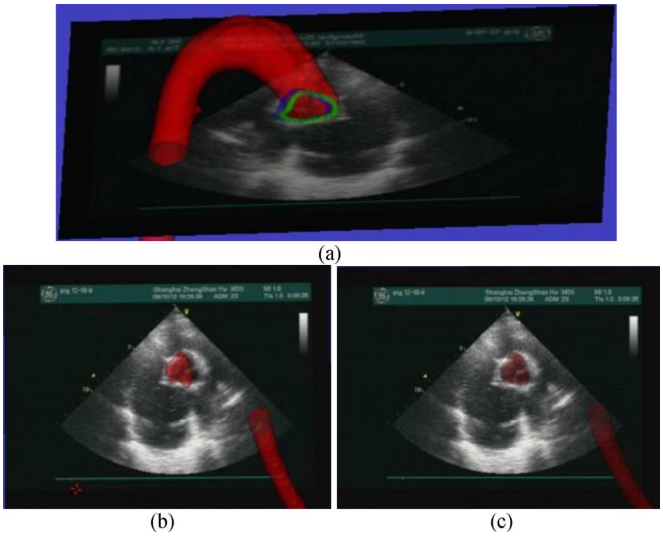
(a) (b) (c)

Fig. 8. Registration of the contour, automatically extracted from the US image intra-operatively, to the preoperative dynamic aortic model. (a) The blue point set represents the contour while the green points show the result of matching the blue set registered to the aortic model using ICP registration. (b) Before ICP registration, we can see clearly the mis-registration between the US image and the aortic model. (c) After ICP registration, the US image and aortic model overlap well.

where $D_p$ is the distance from pixel $p$ in $A$ to $C$, $D_p^i$ is the distance from the corresponding pixel of $p$ in *prior* image $i$ to the center of *prior* image $i$, $I_p$ is the intensity of $p$ and $I_p^i$ is the intensity of $p$ in *prior* image $i$. $D_p(D_p^i)$ and $I_p(I_p^i)$ are normalized by $D_{\max}$ and $I_{\max}$, respectively. The *prior* image with the maximum SM with respect to the current US image was used to extract the contour of the aortic root. Assume that *prior* image $j$ has the maximum SM, in which case $I_F^j$ and $I_B^j$ are used by the current US image to construct the initial data energy terms $C_s$ and $C_t$ as defined by (8) and (9). The GPU based continuous max flow algorithm is then employed to segment the image, resulting in image $g$, as shown in Fig. 7(d). The bounding box of the segmentation operation is obtained by translating the contour of the previously acquired image with a maximum SM, by the vector from the center of the *prior* contour to the center computed from the current US image, and the probability map of the current US image is updated by using the probability function of *prior* image $j$.

*Postprocessing Operations:* Open and close operations are performed on $g$ in sequence to remove the small foreground regions and background holes to obtain image $g1$ [Fig. 7(e)]. *g1* is then multiplied by the probability map of the current US image to remove the region surrounding the aortic root and obtain the image $g2$, as shown in Fig. 7(f). A threshold (0.05 in our application) is used to threshold $g2$ and a binary image $g3$ is obtained [Fig. 7(g)]. The open and close operations are also performed at $g3$ [Fig. 7(h)]. The connected region $A1$ with largest square in $g3$ is recognized as the aortic root. An erosion operation is performed on $A1$ to get a region $A2$. The contour of the aortic region is obtained by subtracting $A2$ from $A1$ [Fig. 7(i)].

### *F. Registration*

Registration between the 2-D intra-operative US image and the preoperative dynamic aortic model is used to compensate for the error caused by respiration and the movement of the aortic root.

Most intensity-based registration algorithms are formulated as optimization problems, where a global optimal transformation between two images is calculated using a specific similarity metric such as mutual information (MI) [28]. On one hand, the selection of an appropriate starting point strongly influences the speed of convergence to a global minimum. We therefore initially choose a registration starting point in the neighborhood of the optimal solution (correct registration) to improve the convergence rate. On the other hand, the low quality of the US image may complicate and prolong the registration process. Hence, we use feature-based registration based on the feature (contour) extracted from intra US image.

The registration procedure, which is based on the framework described by Huang *et al.* [18], consists of two steps: 1) peri-operative registration, 2) intra-operative registration. Fig. 8 shows the result of one of the registrations. The peri-operative registration can be considered as a good starting point for the feature based intra-operative registration, a step which greatly contributes to the optimization procedure (our previous research [21] demonstrates that the TRE is about 4–5 mm).

*1) Peri-Operative Registration:* For this step, a fiducial landmark registration is performed to minimize the mean-squared distance between homologous landmarks in the preoperative CT image and those of the patient (i.e., tracking system (TS) space) to get an initial transform $\mathrm{TM}_{\mathrm{CT}\leftarrow\mathrm{TS}}$. To minimize the heart motion artifacts, we choose the end-diastolic (ED) image of the 4-D dataset for this operation. Since the heart remains relatively stationary with respect to the thoracic cage during the surgery, we expect $\mathrm{TM}_{\mathrm{CT}\leftarrow\mathrm{TS}}$ to be close to the optimal solution. We obtain a series of US images of the aortic root at short and long axis views, along with their cardiac phases. Each of the US images corresponds to a preoperative aortic model defined by its cardiac phase. To obtain a better initial transform, every aortic model corresponds to at least one long axis US image and one short axis view. The contour of the aortic root in each US image is manually selected, and the points of all contours are transformed to preoperative image coordinates using $\mathrm{TM}_{\mathrm{CT}\leftarrow\mathrm{TS}}\mathrm{TM}_{\mathrm{TS}\leftarrow\mathrm{US}}$, where $\mathrm{TM}_{\mathrm{TS}\leftarrow\mathrm{US}}$ is the transformation from 2-D US image coordinate to TS space. This process results in 10 groups of contours with their corresponding cardiac phases related to their respective aortic surface models. All the synchronized pairs of transformed aortic root contours and surface models are then registered using a feature based iterative closest point (ICP) [29] registration to obtain the transforms $\mathrm{TM}_i (i = 1, \ldots, 10)$. For each preoperative aortic model image, we have a transform $\mathrm{TM}_i^{'} (= \mathrm{TM}_i \mathrm{TM}_{\mathrm{CT}\leftarrow\mathrm{TS}})$, which maps the patient coordinate to the preoperative image coordinate. Since $\mathrm{TM}_i^{'}$ is in the neighborhood of the optimal solution, it is employed as an initial transformation for intra-operative registration.

The contour of the aortic root was manually segmented from frozen US image during peri-operative registration. The patient was immobilized on the operating table and anesthetized before the acquisition of the US images. Since the respiration of patient was also controlled by a mechanical ventilator, the influence of patient motion was not significant.

*2) Intra-Operative Registration:* After peri-operative registration is complete, aortic root contours of the US images are roughly registered to the preoperative images (dynamic aortic model). In each registration, each input short axis view US images is associated with its corresponding cardiac phase $i$, at which the aortic contour is extracted. If we assume that the cardiac phase of the contour is the same as that of the preoperative CT image, the points of the contour are transformed by $\mathrm{TM}_i^{'} \mathrm{TM}_{\mathrm{TS}\leftarrow\mathrm{US}}$ and are registered to the surface model at phase $i$ using the ICP algorithm to obtain a new transform $\mathrm{TM}_i^{''}$. The transform $\mathrm{TM}_i^{''} \mathrm{TM}_i^{'}$ is used frequently during the navigation procedure to update the initial transform. The ICP procedure is parallelizable and can be implemented on a GPU to accelerate the process.

### *G. System Components*

*Transcatheter Aortic Valve Prosthesis:* The transcatheter aortic valve prosthesis (MicroPort, Shanghai, China) is a self-expanding valve comprising a nitinol stent frame with porcine pericardial leaflets. The frame expands to its design dimensions at normal temperature, but can be compressed in ice water to fit inside a catheter. Its components are demonstrated in Fig. 2.

*Catheter:* An 18F catheter (MicroPort, Shanghai, China) was used to deliver the aortic valve prosthesis. As shown in Fig. 9, two 5DOF sensors are embedded in the front part of the catheter. The prosthesis is compressed and embedded into the catheter between the two sensors, so that the MTS can track the position and orientation of the prosthesis when the catheter is inserted into the aorta.

*Tracking Device:* An Aurora MTS (North Digital, Waterloo, ON, Canada) was employed to track the position and orientation of the catheter, the cannula, and the US probe. The root mean square accuracies of the magnetic tracking system were 0.69 mm for 5-D sensor and 0.46 mm for 6-D sensor respectively using an NDI-provided calibration phantom.

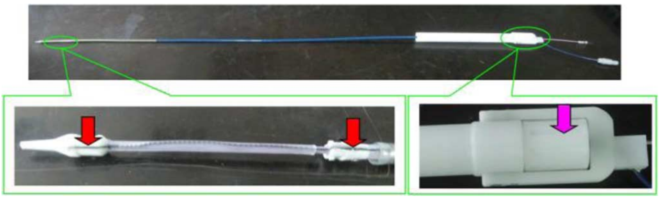

Fig. 9. Catheter used in this study. Two red arrows indicate the location of the 5-D sensors. Pink arrow indicates the knob to release the aortic valve prosthesis.

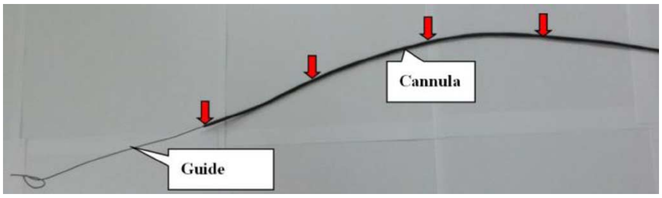

Fig. 10. Guide wire and cannula. Four red arrows indicate the locations of the 5DOF sensors in the cannula. After defining the positions (equally spaced over 10 cm from tip of the cannula) along the cannula, the MTS sensors were mounted and wrapped by a thin plastic coating.

*Guide Wire and Cannula:* Prior to the insertion of the catheter containing the prosthesis, a guide wire is advanced from the common femoral artery to obtain access to the aortic root. The guide-wire is enclosed by a cannula, in front of which four MTS 5DOF sensors are embedded to enable tracking (Fig. 10). The positions of these four sensors are used to fit a cardinal spline to create a model of the front part of the cannula that can be displayed in the AR environment, allowing the interventionist to track the cannula as it passes through the aortic arch. When the cannula arrives at the aortic root, it is extracted, while the guide wire remains, and the catheter is then inserted into the aorta along the guide wire until it arrive at the aortic root.

*ECG Recording:* A simple ECG recorder (Beijing Choice Electronic Tech, Beijing, China) was used intra-operatively to sample the cardiac phase of the subject.

*Ultrasound Machine:* In our research, we used a GE Vivid 7 US machine (General Electric Company, New York, USA) to acquire real-time 2-D US images of porcine subjects using a M3S GE Vivid 7 transducer probe with field of view 90° and depth of field of 15 cm. A 10 moons HDV3000E video capture card (10 moons Technology Development, Huizhou, China) was used as the frame grabber to acquire US images from the US machine with image resolution 320 × 240.

*Software:* The software for this system was based on our previously developed cardiac navigation system [30] using Python 2.7, and third-party libraries from the Visualization Toolkit: VTK 5.6 (http://www.vtk.org), Atamai (http://www.atamai.com) and Compute Unified Device Architecture (CUDA 4.0). The system runs under Windows XP, on an Intel Core i7 computer with an NVIDIA GeForce GTX 560 graphics card with 1 GB display memory and 256 bit data width. Subsequent to probe calibration, the US images acquired via a frame-grab from the GE Vivid 7 US machine, were transferred into our navigation system.

The application software in our system involves five tasks running in parallel on individual threads.

1) The main thread is responsible for acquiring the latest transformation from the registration thread, applying it to the current real-time 2-D US frame and displaying the 4-D aortic surface model of patient. This model is overlaid with the transformed US images to construct an augmented reality (AR) environment that provides an updated interior view of the aorta in real-time. The most recent transformation is used to update the model of the prosthesis and to monitor the distance from the target position to the prosthesis after insertion of the catheter into the aorta.
2) The US acquisition thread acquires 2-D US images from the US machine and stores them in a public buffer.
3) The ECG acquisition thread acquires real-time ECG signals of the subject from the ECG recorder via a serial port, analyzes the corresponding cardiac phase from the current input ECG signal, and stores the cardiac phase in a public buffer.
4) The synchronization thread synchronizes the US image and ECG signals, sending the synchronized US image, cardiac phase and spatial tracking information to the registration thread for each update.
5) The registration thread is employed to rapidly align the preoperative dynamic aortic model with intra-operative 2-D US images. It receives the synchronous US image, cardiac phase, and spatial tracking information from the synchronization thread, and extracts the contour of the aortic root from the input US image. It also employs the ECG signals to synchronize the real-time 2-D US image with the dynamic aortic model, and then spatially aligns the extracted contours of the paired 2-D US and 3-D CT images. Once the temporal and spatial registration is completed, the resulting transformation is sent to the main thread.

### *H. Navigation*

After preoperative planning, US probe calibration, and registration, the prosthesis and target plane are displayed in an augmented reality (AR) environment of the navigation system, as shown in Fig. 11. The target plane is depicted in purple, while the blue line segment perpendicular to the target plane represents the distance from the top point of the folded aortic valve prosthesis to the target plane. $a$ represents the angle between the normal of the target plane and the direction of aortic valve prosthesis. The navigation system monitors and reports this distance and angle throughout the procedure to guide the deployment. The angle information provided by the guidance system in real time allows the tilt to be controlled. During the procedure, the 5DOF sensors provide an intuitive depiction of the orientation and position of the prosthesis in the aorta.

### *I. Validation*

*Evaluation of Aortic Root Contour Extraction:* The aortic root contour is extracted so that it may be registered to the dynamic aortic model in real-time. The accuracy and speed of this operation are crucial to the intra-operative registration.

*1) Accuracy:* We use distance-based metrics [31] to measure the difference between the generated and "true" contours ($G$ and $T$) of the aortic root. $G$ and $T$ are defined by two sets of vertices $G = \{g_i : i = 1 \ldots K\}$ and $T = \{t_i : i = 1 \ldots N\}$ respectively, the distance between $g_i$ and $T$, is defined as

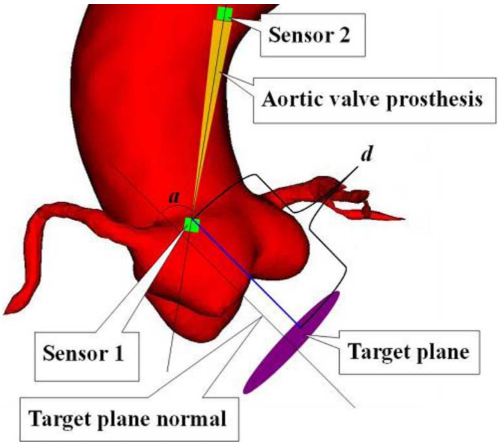

Fig. 11. Layout of the navigation procedure. Blue line segment perpendicular to the target plane represents the distance *d* from the top point of the folded aortic valve prosthesis to the target plane, and *a* represents the angle between the normal of target plane and the direction of aortic valve prosthesis.

$$d(g_i, T) = \min_{t \in T} \|g_i - t\| \tag{14}$$

where $\|g_i - t\|$ is the Euclidean distance between $g_i$ and $t$. For each image, we compute the mean absolute difference (MAD) (15) and the maximum difference (MAXD) (16)

$$\mathrm{MAD} = \frac{1}{K} \sum_{i=1}^{K} d(g_i, T) \tag{15}$$

$$\mathrm{MAXD} = \max_{i \in [1,K]} \{d(g_i, T)\}. \tag{16}$$

For completeness, the area-based metric (AM) is also reported as an overlap measure for the contour segmentation. AM is defined as

$$\mathrm{AM} = \frac{A_{G \cap T}}{A_T} \tag{17}$$

where $A_{G \cap T}$ is the square of the intersection between $G$ and $T$, $A_T$ is the square of $T$.

*2) Speed:* We measure the time to extract the aortic root from a short axis US image.

*Animal Study:* The system was validated in six porcine studies in which four different errors were measured during prosthesis deployment. This study was performed with the approval of the Committee of Research Ethics of Shanghai Jiao Tong University.

*3) Fiducial Registration Error (FRE):* FRE was assessed in each case by calculating the root mean square of the difference between the fiducial marker positions in image space, and their registered positions in world coordinates [32]. FRE is defined by

$$\mathrm{FRE} = \frac{1}{N} \sum_{i=1}^{N} |Tx_i - y_i| \tag{18}$$

where $N$ is the number of source points, and $T$ is the transform between the world coordinates and the preoperative CT image. The fiducial registration algorithm finds the transform $T$ that minimizes the FRE. The FRE is reported by the navigation system automatically after registration.

*4) Target Registration Error (TRE):* TRE defines the misregistration error between the tracked device location reported by the system, and its actual location, compared to a postoperative CT image that is employed as ground truth. Since the postoperative CT must be realigned to the preoperative image to ensure consistency with the tracking system coordinate, the errors introduced by using the postoperative CT image arise only from the registration procedure.

TRE is measured by advancing the tracked cannula from the common femoral artery access to the aortic root after registering the pig's preoperative 4-D CT images to world coordinates using the registration method described above. The locations $p_{\text{navi}}^{i,j}$ $(i = 1, 2, 3, 4;\ j = 1, 2, \ldots, N$, where $N$ is the number of phases in a cardiac cycle) of the four sensors in each phase of a cardiac cycle are reported by the system. We then fixed the cannula inside the aorta and the postoperative 4-D CT images were acquired. For each pair of pre- and postoperative images we performed a rigid registration using the fiducial landmarks to obtain an initial transformation. Based on the transformation, a MI registration was employed to refine the registration from the postoperative to the preoperative image to achieve the final transformation $\text{TM}_j$. Because the sensors can be easily identified in the CT image, their positions $p_{\text{post}}^{i,j}$ in the postoperative image coordinate system were measured and considered as the ground truth. For each cardiac phase $j$, we transformed the $p_{\text{post}}^{i,j}$ to their preoperative equivalents using $p_{\text{pre}}^{i,j} = \text{TM}_j p_{\text{post}}^{i,j}$, where $p_{\text{pre}}^{i,j}$ are the fiducial positions in the preoperative image coordinate system. The TRE for each cardiac phase is then computed by

$$\text{TRE}_j = \frac{1}{M} \sum_{i=1}^{M} \left| p_{\text{pre}}^{i,j} - p_{\text{navi}}^{i,j} \right| \tag{19}$$

where $M$ is the number of sensors in the cannula.

Since the postoperative CT is realigned to the preoperative image, and is thus consistent with the tracking system coordinate system, the errors introduced using postoperative CT image only occur during the registration procedure.

*5) Deployment Distance Error (DDE):* DDE is defined as the difference between actual final prosthesis position and that planned preoperatively, and is measured as the distance between the leading edge of the prosthesis to the target plane in the postoperative CT coordinate system.

*6) Deployment Tilting Error (DTE):* DTE is employed to evaluate how well the system can position the valve in the aortic root anatomy with a correct angulation [33]. DTE is measured as the angle between the target plane normal and the normal of the plane defined by the leading edge of the prosthesis in the postoperative CT coordinate system.

## III. RESULT

### *A. Evaluation of Aortic Root Contour Extraction*

To establish a gold standard contour, we manually segmented the short-axis aortic root US image. We evaluated the aortic root contour extraction on these images (resolution 320 × 240) from 10 patients and five pigs (150 images in total) with the overall performance of the extraction algorithm being summarized in Table I, with representative results shown in Fig. 13. Algorithmically segmented contours correspond well with those segmented manually, with a MAD of 0.92±0.85 mm, a MAXD of 1.71±0.68 mm and an AM of 94.73±3.47%.

The run-time for the extraction of the contours was 36.13±6.26 ms.

TABLE I
SEGMENTATION EVALUATION

| MAD | MAXD | AM | Run time |
|---|---|---|---|
| 0.92±0.85 | 1.71±0.68 | 94.73±3.47 | 36.13±6.26 |

MAD and MAXD are measured in mm, AM in % and Run time is measured in ms. N = 150 (10 patients and 5 pigs, 10 samples throughout cardiac cycle.)

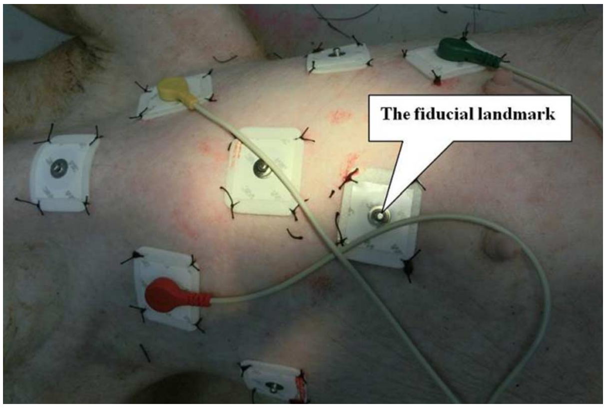

Fig. 12. Fiducial landmarks are ECG electrodes attached uniformly on the skin in the area of the rib-cage to perform the initial registration.

### *B. Animal Study*

Pigs weighing between 60–70 kg were selected for the experiments. Eight fiducial landmarks (ECG electrodes) were attached evenly on the skin in the area of the rib-cage (Fig. 12). The animals were anaesthetized and the heart rate reduced to 90–100 beats/min by injected Betaloc (5 mg:5 ml, Vetter Pharma-Fertigung Gmbh CoKG, Germany) during the procedure. Respiration was controlled at 15–20 cycles/min by a mechanical ventilator. To eliminate the interference to the magnetic tracking system due to the metallic objects, most metallic objects were removed from the surgical field.

The preoperative dynamic aortic models from the animal studies were reconstructed using the method described earlier, following importation into the navigation system. The preoperative planning was performed on the models to determine the target position of the prosthesis.

To relate the US image coordinates to that of the tracked device, a freehand 3-D US probe calibration was performed [34] using a custom designed calibration phantom described in our previous work [22]. The resulting tracked ultrasound images were then aligned to the CT scan using the registration described above. The tracked guide-wire was then advanced from the common femoral artery access to the aortic root under guidance of the MTS. When the cannula arrived at the aortic

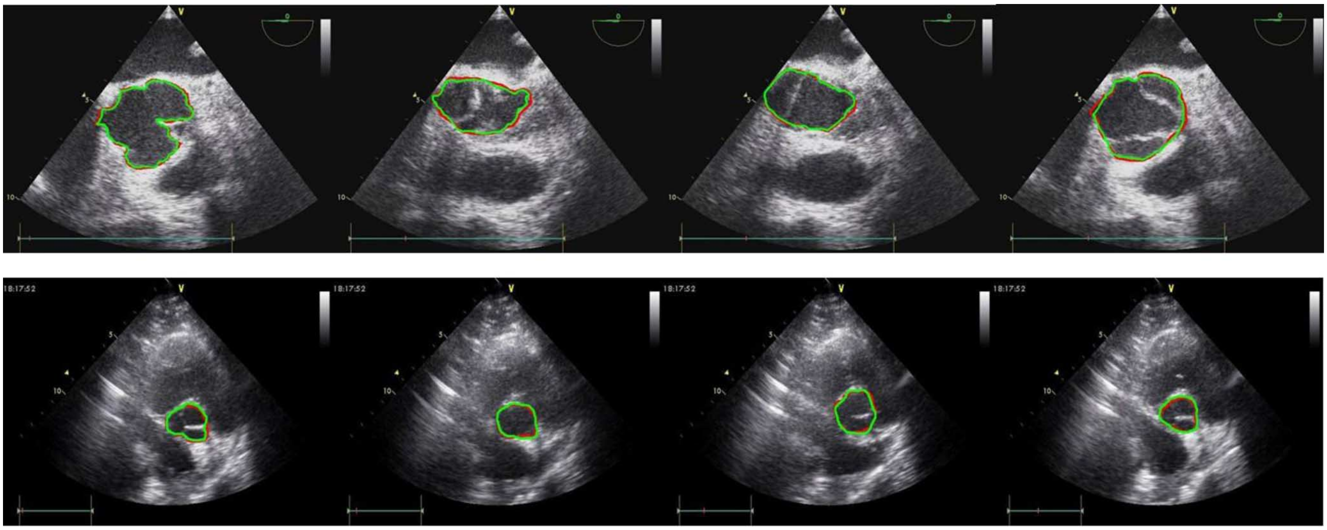

Fig. 13. Segmentation results showing four points in the cardiac cycle for one human and one pig. The red line represents the gold standard manual segmentation, while the green line represents the contour extracted by the algorithm.

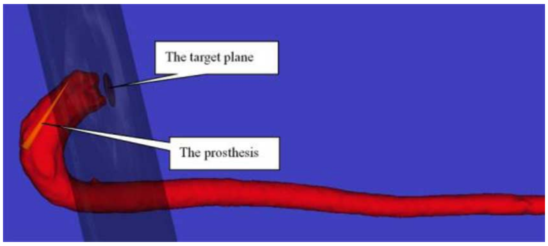

Fig. 14. Guidance system. During the navigation, the real-time US image is registered to the preoperative CT image, fused with the dynamic aortic model and displayed in real-time together with a representation of the tracked prosthesis.

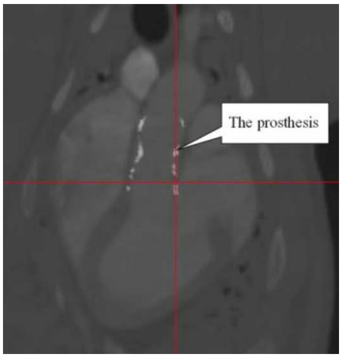

Fig. 15. Postoperative evaluation. Post-operative CT image shows the deployed stent placed successfully in the Aortic Arch. DDE and DTE (the actual distance between the position of the prosthesis and the target position, and the angle between the target plane normal and the normal of the plane defined by the leading edge of the prosthesis, respectively), were measured in this postoperative image.

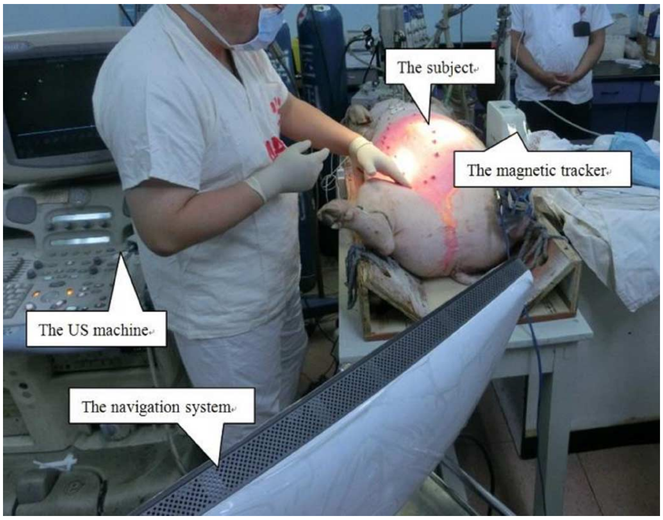

Fig. 16. Experimental setup.

TABLE II
FRE RESULTS (MM)

| | Case1 | Case2 | Case3 | Case4 | Case5 | Case6 |
|---|---|---|---|---|---|---|
| FRE | 3.2 | 1.9 | 3.5 | 4..3 | 2.4 | 4.1 |

root along with the guide wire, the former was removed. Subsequently the catheter was advanced, via the guide-wire, into the aorta. Under the guidance of the system, using registration between the real time US image and preoperative dynamic aortic model (Fig. 14), the interventionist was able to confidently reach the target position and release the valve prosthesis to its correct position. After the procedure, the postoperative CT image (Fig. 15) was examined to determine the DDE and DTE. Although the preoperative preparations procedures are quite different between the two approaches, the workflow during the intervention is quite similar. The major difference is on the guidance method. Figs. 16 and 17 show the experimental setup and the flowchart of the whole procedure, respectively. The FRE is 3.02±0.39 mm (Table II), the TRE 3.31±1.55 mm (Table III), the DDE 3.23±0.94 mm (Table IV) and DTE 5.85±3.06° (Table IV).

## IV. DISCUSSION

### A. *Calculation of Cardiac Phase From ECG Signals*

For the algorithm of computing the cardiac phase, it seems that the R wave can be detected just as the maximum of the magnitude of the ECG signal. In our application, the maximum of

TABLE III
TRE RESULTS (MM)

| Case | Phase1 | Phase 2 | Phase3 | Phase4 | Phase5 | Phase6 | Phase7 | Phase8 | Phase9 | Phase10 |
|---|---|---|---|---|---|---|---|---|---|---|
| 1 | 2.95±0.83 | 3.38±1.36 | 4.28±1.86 | 4.18±1.63 | 4.98±2.12 | 2.18±0.64 | 1.83±1.13 | 2.23±0.99 | 3.78±1.41 | 2.68±1.02 |
| 2 | 3.18±1.63 | 2.93±1.59 | 3.83±1.90 | 3.60±1.47 | 4.63±1.31 | 2.33±0.57 | 1.63±0.67 | 1.48±0.64 | 4.18±1.81 | 2.55±1.36 |
| 3 | 3.15±1.25 | 3.07±1.52 | 4.53±1.45 | 4.35±1.70 | 5.18±1.69 | 2.63±0.81 | 1.73±0.49 | 2.33±0.96 | 4.38±1.57 | 2.25±1.16 |
| 4 | 3.55±1.04 | 3.45±1.17 | 4.98±1.42 | 3.83±1.56 | 4.23±0.91 | 2.68±0.91 | 2.52±1.03 | 2.28±1.13 | 4.75±1.16 | 2.52±0.81 |
| 5 | 3.58±1.39 | 3.22±1.98 | 4.17±1.66 | 4.48±1.69 | 4.73±1.32 | 2.15±1.02 | 1.68±0.39 | 1.78±1.31 | 4.67±1.00 | 2.73±0.51 |
| 6 | 3.07±1.39 | 3.43±1.87 | 5.10±1.12 | 4.15±1.59 | 4.68±1.59 | 2.45±0.69 | 1.78±1.07 | 2.43±0.57 | 3.98±1.61 | 3.13±1.50 |

The start point of a cardiac cycle is the R point in ECG.

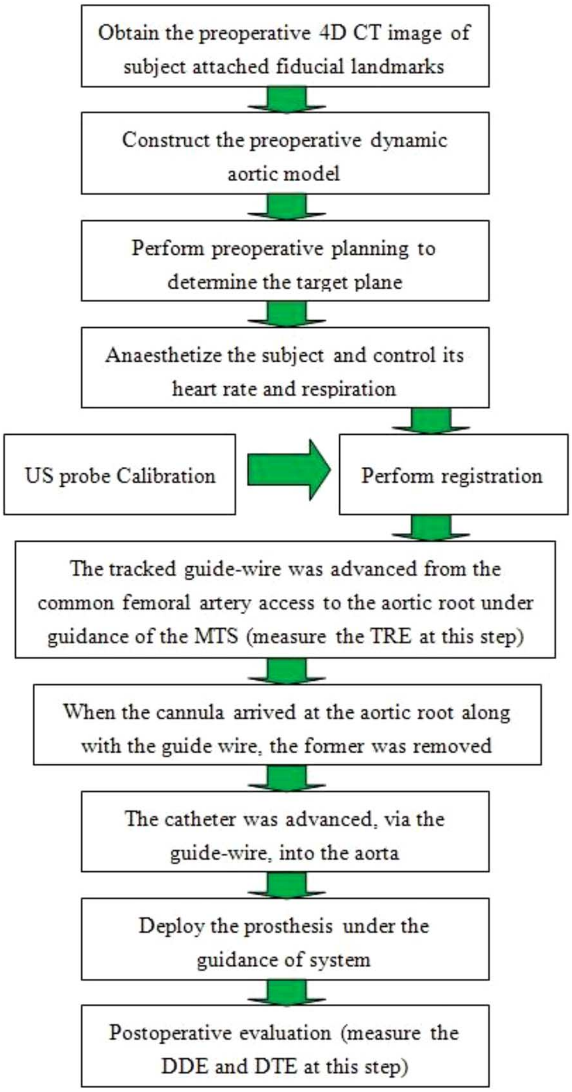

Fig. 17. Flowchart of the whole procedure.

TABLE IV
DDE AND DTE RESULTS

| | Case1 | Case2 | Case3 | Case4 | Case5 | Case6 |
|---|---|---|---|---|---|---|
| DDE (mm) | +2.5 | +3.3 | +2.2 | +4.2 | +2.8 | +3.7 |
| DTE (° ) | 5.3 | 2.3 | 3.1 | 6.2 | 10.7 | 7.5 |

DDE and DTE were measured in mm and degree. The plussymbolin front of the DDE entry indicates that the final position of the prosthesis exceeds the target position in the direction of the LV.

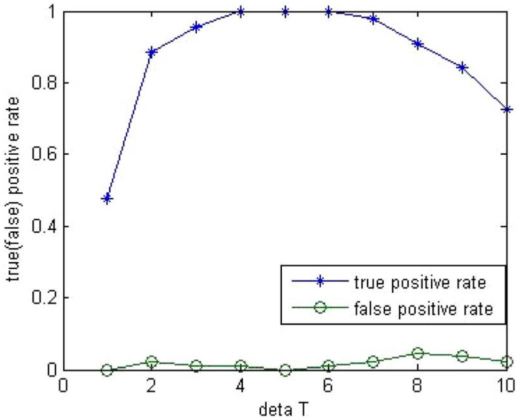

Fig. 18. True positive and false positive rates for different $\Delta t$.

the magnitude of the ECG signal works in most cases. However, the magnitude of the ECG signal may unexpectedly increase during the recording process if the heart rate of the subject is not very stable rendering the predefined threshold invalid. $g(t)$ helps in this case.

As shown by (1), the choice of $\Delta t$ will significantly influence $g(t)$ on which the localization of R depends. To define the optimal $\Delta t$, ECG signals of five subjects, each containing 100 cardiac cycles, were recorded to measure true positive and false-positive rates, defined as the number of correct and incorrect detected R points divided by the actual number of R points contained in the five ECG signals, respectively. The results of different $\Delta t$ are shown in Fig. 18 which demonstrates that $\Delta t = 5$ had both maximal true positive and minimal false positive rates.

## B. Aortic Root Contour Extraction From US Image

Considering the deformation of the aortic root, we used more *prior* US images evenly distributed in a cardiac cycle than reported in [18] and constructed not only a probability function using all *prior* US images but probability functions for each *prior* US image. The probability function is a joint distribution of the intensity $I(x)$ and the distance $R(x)$ relative to the geometric center of the region of interest, which is defined in (6) and (7). Additional 5–7 *prior* US images can effectively represent most states of the opening and closing motion of an aortic valve from approximately 30 images acquired during a single cardiac cycle.

For each input US image, the probability function of the best matched *prior* image was used to construct the probability function of the current input US image, making the construction more accurate (MAD: 0.92±0.85 mm versus 0.95±0.88 mm [20]; average of MAXD:1.71 mm versus 2.33 mm [20]; AM: 94.73±3.47% versus 94.0±0.02% [20]). The run time of the aortic root extraction from the US image is 36.13±6.26 ms, allowing the aortic root contour extraction to be performed in real-time.

### *C. Animal Study*

One major concern of the physicians is whether the magnetic tracking system would be sufficiently accurate in the OR environment. While this is a valid concern, our own experience with the NDI tracking system under normal operating room condition, using the flat table-top field generator on top of the OR table, shows that a typical TRE of 1.16±0.18 mm can be achieved. To avoid interference to the magnetic tracking system, we ensured a magnetically clean environment by eliminating ferrous instruments from the field of view of the magnetic field generator. Testing using the NDI toolbox [35] revealed errors introduced by this source to be minimal. Since the ultrasound probe may be another potential source of disturbance of the magnetic tracking, we employed the NDI toolbox, which can report an error value of the 6DOF sensor indicating how well the transformation was measured, to analyze the interference caused by the US probe. After measuring the errors of the 6DOF sensor alone, and with the ultrasound probe in place, we determined that the presence of the US probe did not significantly increase the error, which is largely attributed to the local magnetic environment rather than the probe itself.

To obtain a clear baseline evaluation of system accuracy independent of the complications introduced by *in vivo* testing, an evaluation of the overall performance of the system under ideal conditions in a bench top setup was performed with a phantom constructed from transparent plastic [21], where a small cube, a bent tube and a straight tube simulates the heart, aorta, and esophagus respectively. The resulting TRE was 1.09±0.15 mm.

Below we report the FRE, TRE, DDE, and DTE errors as measured in the animal study.

TRE represents the actual error of the registration, with the main influencing factors being the specification of the selected points for rigid landmark-based registration in image and real space, co-registration between preoperative and postoperative images, the pivot tracker calibration operation [36], and respiration. The registration algorithm employed in this research is based on ICP, whose accuracy and convergence rate depends on the initial transformation. Since respiratory motion is a major factor influencing the output of the initial registration, to reduce its influence, the ventilator was employed to control respiration. Lang *et al.* [20] extracted the aortic root contour from the intra-operative US image and registered this contour to the preoperative aortic model. However, in their work, only a static aortic model was employed for the registration, without compensating for its movement. Our registration between the intra-operative US image and dynamic aortic model achieved a better result (TRE is 3.31±1.55 mm versus 5.90±3.22 mm in [20]). Results in Table IV demonstrate that it is more robust to register US and CT images at diastole due to fewer motion artifacts, and specifically at mid-diastole to obtain optimum accuracy across the cardiac cycle. In practice, since the cannula and catheter are moved slowly within the aorta during the procedure, it is feasible to register the US and CT images at diastole and apply the resultant transformation throughout the cardiac cycle.

The DDE and DTE measure the overall accuracy of the system, while the FRE and TRE contribute to these parameters. The DDE measured in our work was 3.23±0.94 mm. The result in Table IV shows that the prosthesis deviated towards the LV in all cases, which we believe to be caused by two factors. First, the prosthesis we used is designed for human use and does not match the porcine morphology exactly, since the diameter of the outflow of the aortic valve prosthesis in humans is much larger than that of the swine's aorta root (sinotubular junction and the adjacent tubular part of the aorta). Subsequently, after the release of the aortic valve prosthesis, the pressure of the vascular wall makes it slide towards the LV. Secondly, in humans the calcification of the aortic valve (the principal cause of valve failure in the first place), helps to fix the aortic valve prosthesis in the aorta. However the porcine subjects have healthy valves without calcification. The DDE for existing X-ray guided TAVI is at least 4.8 mm [37], [38], whereas we achieved 3.23±0.94 mm without fluoroscopy. This can be considered a clinically acceptable result. For the DTE, a tilting of less than 5° is regarded as very good, 5°–10° as good, 10°–15° as acceptable, and larger than 15° as unacceptable [33]. The DTE of our study is 5.85±3.06°, where one case was within 10°–15°, three within 5°–10°, and two less than 5°. The DTE of fluoroscopic guidance is 5°–10°. Moreover, the proposed approach requires five clinicians (two cardiac intervention physicians with more than five years experience with TAVI and who performed the valve deployment, one cardiac surgeon, one US physician and one anesthetist) during the whole procedure, where the standard TAVI procedure needs six clinicians (one more radiologist). The procedure time is less than 75 min except for the time required for dynamic aortic model construction.

Compared to the traditional TAVI, our approach requires an additional magnetic tracking system with an adaptive surgical environment without metal and a US machine. Since TEE also is already used during traditional TAVI for monitoring and evaluation of valve deployment, this does not represent additional cost. Moreover, the capital and operating costs of the X-ray machine are eliminated.

The risk of peri-procedural death remains significant, at 5.0% after 30 days, and the majority of TAVI complications are related to poor positioning of the valve at the time of deployment [39]. We were unable access any detailed guidelines relating to the desired clinical accuracy, but in our experience, an error of less than 5 mm is considered by the interventionist community to be sufficient. We believe the more accurate placement shown in our experiment will improve outcomes compared to X-ray guided TAVI.

The aortic model is animated during the entire procedure, which introduces a small latency into the final presentation of the model to the clinician. Since each static aortic model was constructed by surface rendering and each model contained fewer than 20 000 meshes, this latency was insignificant. The major latency was caused by the sum of temporal synchronization and intra-operative registration delays. The system updates the model after the contour, extracted from synchronized intra-operative US image, is registered to the corresponding

**ALGORITHM 1** CALCULATE CARDIAC PHASE OF ECG SIGNALS

```
Initialize:
Initialize the queue Q
Read ECG signals and add them into the Q until Q is full

for each element i of Q do
    if $\triangle t \leqslant i \leqslant N-\triangle t$ do
        Compute $g(i)=\frac{(E(i)-E(i-\Delta t))(E(i)-E(i+\Delta t))}{2\Delta t}$, where E(x) is the value of element x representing the magnitude of ECG signal in Q, N is the length of Q.
Get the maximum g(i) as $g_{\max}$
for each element i of Q do
    if $g(i) > 0.9\times g_{\max}$ do
        The element i is recognized and marked as R point
for each adjacent two R points i and j ($i \leqslant j$) do
    Compute the time between the them by T=4 (j-i) ms
Compute the average time of these T as $T_{current}$
$T_{current}$ is considered as the cardiac circle period

Calculate Cardiac Phase :
for each new input data (contains 4 ECG signals) do
    Append the four ECG signals it contained to Q, element N-3 is the first ECG signal in the new input data
    Set k = 0
    while k < 4 do
        Compute $g(N-k-L)=\frac{(E(N-k-L)-E(N-k-L-\Delta t))(E(N-k-L)-E(N-k-L+\Delta t))}{\Delta t^2}$
        if $g(N-k-L) > 0.9\times g_{\max}$ do
            Element N-k-L is recognized and marked as R point
            Find the closest element j marked as R point before element N-k-L
            $T_{current}$ = 4 (N-k-L-j) ms
            Return cardiac phase $\frac{4(k+L)}{T_{current}}\times 100\%$
        k = k+1
    Find the closest element j marked as R point before element N-k-L
    Return cardiac phase $\frac{4(N-j)}{T_{current}}\times 100\%$
```

$\Delta t$, L and N are experience values. In our application, $\Delta t=5$, L = 11 and N = 800.

aortic model. This delay amounts to 120 ms at most, which rarely affects the procedure.

The creation of the dynamic model from preoperative images does require more radiologists' time to segment the aorta in current stage. But it could be improved with a more efficient method. A fast segmentation by the semi-automatic segmentation method [21] proposed in our previous research takes less than 4 min to achieve the aorta in each 3-D image of the preoperative 4-D CT image. The 4-D cardiac CT is becoming more and more widely employed, especially for the cardiac intervention. While our current segmentation procedure is only semi automatic and takes around 4 min, we are aware of proprietary approaches such as that performed by the Siemens Zeego system that are automatic and effectively instantaneous. We currently do not have access to this technology, but it has the potential to be employed in this environment. The use of a manual over an automatic approach does not impact on the overall conclusions of this research.

## V. CONCLUSION

This paper proposed an MTS enabled navigation system for transcatheter aortic prosthesis deployment, using intra-operative US imaging and a dynamic aortic model. The animal studies demonstrate the feasibility of the proposed approach, and that it can be achieved with an accuracy similar to that achieved with a conventional fluoroscopy, without the harmful effects of radiation to the patient during the procedure. Our procedure also benefits from the additional 3-D context achieved through registration of pre-operative 3-D models.

The main obstacle to the clinical realization of this approach is to make the system compatible with the current clinical workflow and to make it convenient for physicians. The current segmentation procedure is still not fully automatic and could be improved. However, we are aware of proprietary approaches such as those performed by the Siemens Zeego system that are automatic and effectively instantaneous. Those approaches may possibly be employed in this environment in our future work. Human experiments will be performed to further validate the proposed approach. We believe this methodology could be feasible for delivery and deployment of aortic valve prostheses in humans in the near future.

## APPENDIX

Algorithm 1 to calculate the cardiac phase in ECG signals.

## ACKNOWLEDGMENT

The authors are grateful to the radiologists from Zhongshan Hospital for their support in animal imaging and animal surgery as well as to MicroPort Co., Ltd. for providing cannulae, catheters and aortic valve prostheses for this project. The authors would also like to thank the reviewers for their valuable suggestions during the revision process for this paper.

## REFERENCES

[1] V. R. Nkomo, J. M. Gardin, T. N. Skelton, J. S. Gottdiener, C. G. Scott, and M. Enriquez-Sarano, "Burden of valvular heart diseases: A population-based study," *Lancet*, vol. 368, pp. 1005–1011, 2006.

[2] R. O. Bonow, B. A. Carabello, K. Chatterjee, A. C. J. Leon, D. P. Faxon, M. D. Freed, W. H. Gaasch, B. W. Lytle, R. A. Nishimura, P. T. O'Gara, R. A. O'Rourke, C. M. Otto, P. M. Shah, and J. S. Shanewise, "Focused update incorporated into the ACC/AHA 2006 guidelines for the management of patients with valvular heart disease: A report of the American College of Cardiology/American Heart Association task force on practice guidelines," *Circulation*, vol. 118, pp. e523–e661, 2008.

[3] B. Iung, A. Cachier, G. Baron, D. Messika-Zeitoun, F. Delahaye, P. Tornos, C. Gohlke-Bärwolf, E. Boersma, P. Ravaud, and A. Vahanian, "Decision making in elderly patients with severe aortic stenosis: Why are so many denied surgery?," *Eur. Heart J.*, vol. 26, pp. 2714–2720, 2005.

[4] M. Chu, M. Borger, F. Mohr, and T. Walther, "Transcatheter heart-valve replacement: Update," *Can. Med. Assoc. J.*, vol. 182, no. 8, pp. 791–795, 2010.

[5] J. Leipsic, R. Gurvitch, T. LaBounty, J. Min, D. Wood, M. Johnson, A. Ajlan, N. Wijesinghe, and J. Webb, "Multidetector computed tomography in transcatheter aortic valve implantation," *J. Am. Coll. Cardiol. Img.*, vol. 4, no. 4, pp. 416–429, 2011.

[6] P. Lang, P. Seslija, M. W. Chu, D. Bainbridge, G. M. Guiraudon, D. L. Jones, and T. M. Peters, "US-fluoroscopy registration for transcatheter aortic valve implantation," *IEEE Trans. Biomed. Eng.*, vol. 59, no. 5, pp. 1444–1453, May 2012.

[7] V. Delgado, A. Ng, M. Shanks, F. Van Der Kley, J. Schuijf, N. Van De Veire, L. Kroft, A. Roos, M. Schalij, and J. Bax, "Transcatheter aortic valve implantation: Role of multimodality cardiac imaging," *Expert Rev. Cardiovasc. Ther.*, vol. 8, no. 1, pp. 113–123, 2010.

[8] R. K. Greenberg, S. Haulon, S. O'Neill, S. Lyden, and K. Ouriel, "Primary endovascular repair of juxtarenal aneurysms with fenestrated endovascular grafting," *Eur. J. Vascul. Endovascul. Surg.*, vol. 27, pp. 484–491, May 2004.

[9] D. Tarek, "An evidence-based approach to minimise contrast-induced neuropathy," *J. New Zealand Med. Assoc.*, vol. 122, pp. 39–41, Jul. 2009.

[10] G. Lauritsch, J. Boese, L. Wigström, H. Kemeth, and R. Fahrig, "Towards cardiac C-arm computed tomography," *IEEE Trans. Med. Imag.*, vol. 25, no. 7, pp. 922–934, Jul. 2006.

[11] J. Kempfert, A. Rastan, A. Noettling, J. Blumenstein, A. Linke, F. Schule, R. G. Mohr, and T. Walther, "Perioperative dynact for improved imaging during transapical aortic valve implantation," *Circulation*, vol. 122, no. 21S, Nov. 2010.

[12] P. Mountney, R. Ionasec, M. Kaizer, S. Mamaghani, W. Wu, T. Chen, M. John, J. Boese, and D. Comaniciu, "Ultrasound and fluoroscopic images fusion by autonomous ultrasound probe detection," in *Proc. MICCAI*, 2012, vol. 7511, pp. 544–551.

[13] P. Wang, T. Chen, O. Ecabert, S. Prummer, M. Ostermeier, and D. Comaniciu, "Image-based device tracking for the co-registration of angiography and intravascular ultrasound images," in *Proc. MICCAI*, 2011, vol. 6891, pp. 161–168.

[14] K. Horvath, D. Mazilu, M. Guttman, A. Zetts, T. Hunt, and M. Li, "Midterm results of transapical aortic valve replacement via real-time magnetic resonance imaging guidance," *J. Thoracic Cardiovasc. Surg.*, vol. 139, no. 2, pp. 424–430, 2010.

[15] K. Horvath, D. Mazilu, O. Kocaturk, and M. Li, "Transapical aortic valve replacement under real-time magnetic resonance imaging guidance: Experimental results with balloon-expandable and self-expanding stents," *Eur. J. Cardio-Thoracic Surg.*, vol. 39, no. 6, pp. 822–828, 2011.

[16] F. Manstad-Hulaas, S. Ommedal, G. A. Tangen, P. Aadahl, and T. N. Hernes, "Sidebranched AAA stent graft insertion using navigation technology: A phantom study," *Eur. Surg. Res.*, vol. 39, no. 6, pp. 364–371, 2007.

[17] N. Abi-Jaoudeh, N. Glossop, M. Dake, W. F. Pritchard, A. Chiesa, M. R. Dreher, T. Tang, J. W. Karanian, and B. J. Wood, "Electromagnetic navigation for thoracic aortic stent-graft deployment: A pilot study in swine," *J. Vascul. Intervent. Radiol.*, vol. 21, no. 6, pp. 888–895, 2010.

[18] X. Huang, J. Moore, G. Guiraudon, D. L. Jones, D. Bainbridge, J. Renand, and T. M. Peters, "Dynamic 2-D ultrasound and 3-D CT image registration of the beating heart," *IEEE Trans. Med. Imag.*, vol. 28, no. 8, pp. 1179–1189, Aug. 2009.

[19] C. H. Huber, M. Nasratulla, M. Augstburger, and L. K. Von Segesser, "Ultrasound navigation through the heart for off-pump aortic valved stent implantation: New tool," *J. Endovasc. Therapy*, vol. 11, pp. 503–510, Aug. 2004.

[20] P. Lang, M. Rajchl, A. J. McLeod, M. W. Chu, and T. M. Peters, "Feature identification for image-guided transcatheter aortic valve implantation," in *Proc. SPIE Med. Imag. Conf.*, 2011, vol. 8316, pp. 83162X-1–83162X-14.

[21] Z. Luo, J. F. Cai, S. Wang, Q. Zhao, T. M. Peters, and L. Gu, "Magnetic navigation for thoracic aortic stent-graft deployment using ultrasound image guidance," *IEEE Trans. Biomed. Eng.*, vol. 60, no. 3, pp. 862–871, Mar. 2013.

[22] Z. Luo, J. F. Cai, and L. Gu, "A pilot study on magnetic navigation for transcatheter aortic valve implantation using dynamic aortic model and US image guidance," *Int. J. Comput. Assist. Radiol. Surg.*, vol. 8, no. 4, pp. 677–690, 2013.

[23] W. E. Lorensen and H. E. Cline, "Marching cubes: A high resolution 3-D surface construction algorithm," in *Proc. SIGGRAPH Comput. Graphics*, 1987, vol. 21, no. 4, pp. 163–169.

[24] F. T. Chan, S. Esedoglu, and M. Nikolova, "Algorithms for finding global minimizers of image segmentation and denoising models," *SIAM J. Appl. Math.*, vol. 66, no. 5, pp. 1632–1648, 2008.

[25] J. Yuan, E. Bae, and X. C. Tai, "A study on continuous max-flow and min-cut approaches," in *Proc. IEEE Comput. Soc. Conf. Comput. Vis. Pattern Recognit.*, 2010, pp. 2217–2224.

[26] M. Rajchl, J. Yuan, E. Ukwatta, and T. M. Peters, "Fast interactive multi-region cardiac segmentation with linearly ordered labels," in *Proc. IEEE Int. Symp. Biomed. Imag.*, May 2012, pp. 1409–1412.

[27] N. Otsu, "A threshold selection method from gray-level histogram," *IEEE Trans. Syst. Man Cybern.*, vol. 9, no. 1, pp. 62–66, Jan. 1979.

[28] F. Maes, D. Vandermeulen, and P. Suetens, "Medical image registration using mutual information," *Proc. IEEE*, vol. 91, no. 10, pp. 1699–1721, Oct. 2003.

[29] P. Besl and N. McKay, "A method for registration of 3-D shapes," *IEEE Trans. Pattern Anal. Mach. Intell.*, vol. 14, no. 2, pp. 239–256, Feb. 1992.

[30] J. F. Cai, Z. Luo, L. Gu, R. Xu, and Q. Zhao, "The implementation of an integrated computer-assisted system for minimally invasive cardiac surgery," in *Int. J. Med. Robot. Comput. Assist. Surg.*, 2010, vol. 6, pp. 102–112.

[31] A. Fenster and B. Chiu, "Evaluation of segmentation algorithms for medical imaging," in *Proc. 2005 IEEE Eng. Med. Biol. 27th Annu. Conf.*, 2005, pp. 7186–7189.

[32] D. D. Frantz, A. D. Wiles, S. E. Leis, and S. R. Kirsch, "Accuracy assessment protocols for electromagnetic tracking systems," *Phys. Med. Biol.*, vol. 48, pp. 2241–2251, 2003.

[33] Y. Zheng, M. John, R. Liao, J. Boese, U. Kirschstein, B. Georgescu, S. K. Zhou, J. Kempfert, T. Walther, G. Brockmann, and D. Comaniciu, "Automatic aorta segmentation and valve landmark detection in C-arm CT: Application to aortic valve implantation," *IEEE Trans. Med. Imag.*, vol. 31, no. 12, pp. 2307–2321, Dec. 2012.

[34] F. Lindseth, G. A. Tangen, T. Langø, and J. Bang, "Probe calibration for freehand 3-D ultrasound," *Ultrasound Med. Biol.*, vol. 29, pp. 1607–1623, 2003.

[35] NDI ToolBox 3.003.006 Northen Digital Inc., Waterloo, ON, Canada.

[36] Programming and application manual Northern Digital, Waterloo, ON, Canada.

[37] J. Kempfert, A. Rastan, A. Noettling, M. John, A. van Linden, J. Blumenstein, A. Linke, G. Schuler, F. W. Mohr, and T. Walther, "Perioperative DynaCT for improved imaging during transapical aortic valve implantation," *Circulation*, vol. 122, p. A16869, 2010.

[38] P. Lang, T. M. Peters, B. Kiaii, and M. W. Chu, "The critical role of imaging navigation and guidance in transcatheter aortic valve implantation," *J. Thoracic Cardiovasc. Surg.*, vol. 143, no. 6, pp. 1241–1243, 2012.

[39] C. R. Smith, M. B. Leon, M. J. Mac, C. Miller, J. W. Mose, L. G. Svensson, E. M. Tuzcu, J. G. Webb, G. P. Fontan, R. R. Makkar, M. Williams, T. Dewe, S. Kapadi, V. Babaliaro, V. H. Thourani, P. Corso, A. D. Pichard, J. E. Bavaria, H. C. Herrman, J. J. Akin, W. N. Anderson, D. Wang, and S. J. Pocock, "Transcatheter aortic-valve implantation for aortic stenosis in patients who cannot undergo surgery," *New Eng. J. Med.*, vol. 363, no. 17, pp. 1597–1607, Oct. 2010.